Earth Planet. Sci. Lett. 673 (2026) 119745

Contents lists available at ScienceDirect

Earth and Planetary Science Letters

journal homepage: www.elsevier.com/locate/epsl

Correlative isotope excursions driven by transport, not global environmental change

Connor S. van Wieren *, Blake Dyer, Jon M. Husson

School of Earth and Ocean Sciences, University of Victoria, Victoria, British Columbia, V8P5C2, Canada

ARTICLE INFO

Editor: H. Bao

Keywords:
Carbonates
Isotope excursions
Carbon isotopes
Sequence stratigraphy
Numerical modeling

ABSTRACT

Carbonate sediments are widely used to reconstruct Earth's climatic and biogeochemical history. While pristine records come from deep-water settings with continuous vertical accumulation, much of the preserved carbonate record originates from shallow platforms, where horizontal transport, erosion, and diagenesis complicate this archive. We develop a numerical sediment transport model tracking the advection of conservative tracers (e.g., $\delta^{13}C$ values of carbonate sediments) to explore the implications of redistribution on sedimentary archives. Results suggest that correlations between $\delta^{13}C$ excursions and their vertical and lateral proximity to sequence boundaries can be explained by erosion and redeposition of older, isotopically distinct carbonate sediments, forming coarse-grained deposits above erosive surfaces. Such isotopic variability may reflect spatial gradients in the dissolved inorganic carbon (DIC) reservoir, with excursion magnitude constrained by the strength of those gradients. Alternatively, these excursions may record redeposition of older sediments, capturing past secular changes in $\delta^{13}C_{DIC}$. We demonstrate that isotope excursions can be duplicated through redeposition, whereby initial shifts in DIC are re-expressed within younger stratigraphy with dampened magnitude. Applying these findings to the Hirnantian carbon isotope excursion (HICE) in Anticosti Island strata, we demonstrate that spatial isotopic gradients within basins will be recorded as excursions within progradational stratigraphy. These excursions will appear synchronous, despite being decoupled from global DIC change. Similar-magnitude $\delta^{13}C$ excursions in coeval strata are often interpreted as evidence for global carbon cycle changes. We show that transport alone can produce such patterns, without invoking global mechanisms. Further, mapping intra-basin $\delta^{13}C$ variability may help distinguish transport from global signals.

1. Introduction

The geochemical composition of shallow-water marine carbonates is often used to reconstruct changes in Earth's biogeochemical cycles, owing in part to their abundance in the sedimentary record. Such changes include shifts in marine temperatures (e.g., Henkes et al., 2018), and major biogeochemical cycles on Earth (Veizer et al., 1999). These inferences are made under the assumption that marine carbonates record the geochemical composition of contemporaneous seawater over geologic time (e.g., Swart, 2008; Geyman et al., 2022). Although open-marine skeletal carbonates best record secular changes in global seawater chemistry (Zachos et al., 2001; Westerhold et al., 2020), subduction limits the deep-ocean record. Consequently, most ancient sediments derive from shallow platforms and epeiric seas, which are geochemically distinct from open-ocean sediments (Swart, 2008). Shallow-water carbonates are influenced by local processes and diagenesis, which can affect the isotopic composition of both local seawater and the carbonates precipitating from it (Allan and Matthews, 1982; Higgins et al., 2018; Ahm et al., 2018), producing geochemical variability independent of secular changes in global marine seawater chemistry.

Changes in the carbon isotopic composition of carbonate sediments ($\delta^{13}C_{carb}$) are frequently used to infer changes in the global carbon cycle. These inferences rely on the observation that marine carbonates typically precipitate in equilibrium with the dissolved inorganic carbon (DIC) pool of the surrounding seawater. It is thought that globally correlatable variations in $\delta^{13}C$ values reflect synchronous shifts in carbon fluxes across Earth's surface reservoirs, processes often associated with major climatic and oceanographic changes (Kump and Arthur, 1999). For example, negative excursions in $\delta^{13}C$ have been linked to organic matter remineralization during rapid warming events (e.g., Zachos et al., 2005) and widespread marine anoxia (Arthur et al., 1987). Moreover, during periods such as the Neoproterozoic Era, when radiometric con-

* Corresponding author.
E-mail address: cvanwier@uvic.ca (C.S. van Wieren).

https://doi.org/10.1016/j.epsl.2025.119745
Received 25 April 2025; Received in revised form 7 November 2025; Accepted 16 November 2025

Available online 20 November 2025

straints are limited and biostratigraphy is unavailable, trends in $\delta^{13}C_{carb}$ are commonly used for inter-basin correlation (e.g., Halverson et al., 2005).

The geochemical composition and preservation of shallow carbonates are shaped by local environmental factors, including early diagenesis. Such influences generate pronounced spatial and facies-dependent variability in $\delta^{13}C_{carb}$ across both modern and ancient systems. On the Great Bahama Bank, $\delta^{13}C_{carb}$ among carbonate components spans nearly 10‰, reflecting environment- and mineralogy-dependent processes (Geyman and Maloof, 2021). Additionally, comparable facies-linked offsets occur in ancient successions such as the Ordovician (Holmden et al., 2024; Yang et al., 2024). Further, 5‰ variability in bulk $\delta^{13}C_{carb}$ has been attributed to unique carbonate components on modern platform tops globally (Brown et al., 2025). On carbonate platforms, erosion, reworking, and transport respond to relative sea-level change and accommodation. When sediment accumulation rates exceed accommodation, the coastline migrates basinward (progradation), resulting in the preferential preservation of shallow, shoreward environments within regressive sequences. Conversely, when accommodation exceeds sedimentation, retrogradation occurs, shifting the coastline landward and preserving deeper, offshore environments within transgressive sequences. These depositional patterns are further modified by sea-level cycles, with carbonate accumulation favored during sea-level highs (highstands) but suppressed during sea-level lows (lowstands). Lowstands can lead to subaerial exposure and platform-wide erosion, producing hiatuses that punctuate the stratigraphic record (Sadler, 1981).

Stratigraphic discontinuities from physical sedimentary processes can disrupt geochemical records. Hiatuses caused by erosion or non-deposition are bounded by correlative surfaces such as transgressive surfaces, marking the shift from regression to transgression, or sequence boundaries formed during sea-level fall, erosion, and exposure (e.g., Algeo, 1996; Caron et al., 2004). Consequently, gradual trends in $\delta^{13}C_{carb}$ may appear as stepwise "jumps" across these boundaries, where parts of the record are omitted or condensed (Strasser, 2015). These stratigraphic gaps distort geochemical signals, complicating interpretation of $\delta^{13}C$ records and precise inter-basinal correlation (e.g., Curtis et al., 2025).

In addition to the effects of depositional architecture and hiatuses, the lateral redistribution of previously deposited carbonate sediments introduces further geochemical complexity into stratigraphic records. Erosion associated with sea-level fall, particularly at sequence boundaries, can remobilize older sediments, which are then transported downslope and re-deposited in deeper settings (e.g., Creveling et al., 2018; van Wieren et al., 2024). When the isotopic composition of these re-deposited sediments differs from contemporaneous carbonates precipitating from local DIC, the eroded wedge of sediment may appear as sharp stratigraphic shifts in $\delta^{13}C_{carb}$ decoupled from secular changes in marine DIC. These sedimentary deposits, hereafter referred to as re-deposited beds, capture and preserve unique geochemical signatures originating from previously deposited and redistributed sediment. This phenomenon is analogous to the "Lazarus Effect" (cf., Flessa and Jablonski, 1983; Jablonski, 1986; Wignall and Benton, 1999), where sedimentary reworking causes taxa to reappear in younger deposits after an apparent absence. Such features complicate the interpretation of geochemical signals and may provide a more parsimonious mechanism for excursions commonly associated with sequence boundaries than invoking global carbon cycle perturbations or diagenesis (e.g., Uličný et al., 1997; Railsback et al., 2003; Jones et al., 2016; Muñoz-López et al., 2025). To explore the influence of sediment transport on stratigraphic proxy records, we present a numerical model that tracks the redistribution of an isotopic tracer representative of carbonate $\delta^{13}C$ ($\delta^{13}C_{carb}$) across a prograding and retrograding carbonate platform. The model captures the effects of spatial isotopic gradients, secular DIC changes, and sea-level oscillations on the stratigraphic expression of geochemical proxies. We assume that $\delta^{13}C_{carb}$ behaves as a conservative tracer that records contemporaneous DIC composition, consistent with standard chemostratigraphic practice based on simple models of the carbon cycle (Kump and Arthur, 1999). Though the effects of diagenesis are clearly important factors in interpreting carbonate archives (Higgins et al., 2018), this assumption allows us to isolate the first-order physical and stratigraphic effects that must be true before any syn- or post-depositional diagenesis has occurred. We then apply these results to the Hirnantian carbon isotope excursion (HICE) of Anticosti Island, Canada (Desrochers et al., 2010; Jones et al., 2011) to illustrate the potential role of sediment transport in producing isotope excursions.

2. Methods

2.1. Model framework & system of equations

Sedimentary transport and the distribution of a conservative tracer within a basin are modeled using a system of two partial differential equations. The first equation is a 1-D diffusion equation applied to topography as shown in Equation (1). Here, h is the modeled topography, t is the model time, x is the spatial coordinate, and K is the sediment diffusivity (a function of water depth z, and the spatial coordinate, x).

$$\frac{\partial h}{\partial t} = \frac{\partial}{\partial x}\left(K\frac{\partial h}{\partial x}\right) \tag{1}$$

Modeling geomorphic processes with hillslope diffusion is widely used in Earth sciences for systems such as fluvial transport, delta progradation, soil creep, and other mass-wasting processes (e.g., Kenyon and Turcotte, 1985; Tucker and Bras, 1998; Salles and Duclaux, 2015). These models assume that sediment flux is proportional to local slope and successfully reproduce stratigraphic patterns such as lithologic distributions in prograding deltas (Rivenæs, 1992) and sediment transport in submarine canyons (Wei et al., 2013). Their mathematical simplicity and computational efficiency make them well suited for simulating sediment transport and landscape evolution over long timescales and large spatial domains. Transport efficiency, driven by processes like wave energy, decays exponentially with water depth and environmental setting (e.g., Kaufman et al., 1991; Rivenæs, 1992); hence, a depth-variant diffusivity is appropriate for modeling shallow-marine, wave-dominated environments where diffusivity drops sharply below the storm-wave base.

To track the advection of a conservative tracer w, which can represent a geochemical proxy such as $\delta^{13}C$, we apply a second 1-D equation (Eqn. (2)) to describe its advection within sediments:

$$\frac{\partial (hw)}{\partial t} = \frac{\partial}{\partial x}\left(Kw\frac{\partial h}{\partial x}\right) \tag{2}$$

Together, Equations (1), and (2) constitute our system of equations. We numerically solve this system using a combination of implicit finite difference approximations and Newton-Raphson iterations as described below.

2.2. Numerical approximations & finite-differencing scheme

For clarity, the following symbolic representations for finite difference approximations are used. Here, i represents the spatial coordinate, and n represents the temporal coordinate. The abbreviated forms for first-order forward and backward difference approximations applied to timestep n are shown in Equations (3) and (4), and the abbreviated equations for first and second-order central difference approximations evaluated at spatial grid-point i are shown in Equations (5) and (6):

$$\Delta_b(a) = \frac{a^{n+1} - a^n}{\Delta b} \simeq \frac{\partial a}{\partial b} \tag{3}$$

$$\nabla_b(a) = \frac{a^n - a^{n-1}}{\Delta b} \simeq \frac{\partial a}{\partial b} \tag{4}$$

$$\delta_b(a) = \frac{a_{i+1} - a_{i-1}}{2\Delta b} \simeq \frac{\partial a}{\partial b} \tag{5}$$

$$\delta_b^2(a) = \frac{a_{i+1} - 2a_i + a_{i-1}}{\Delta b^2} \simeq \frac{\partial^2 a}{\partial b^2} \tag{6}$$

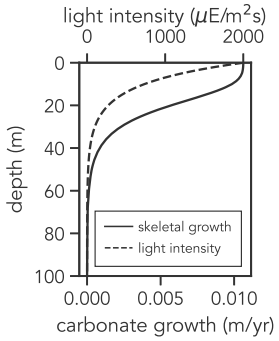

Fig. 1. Production profile for simulated carbonate sediments. Light intensity is shown with the dashed line, and the resulting skeletal carbonate growth is shown with the solid line. Equations are scaled after Bosscher and Schlager (1992).

2.2.1. Treatment of the diffusion equation

To discretize the diffusion equation (Eqn. (1)), we begin by applying a forward difference to our temporal derivatives on the left side, and applying the product rule to the spatial derivatives on the right side:

$$\Delta_t(h) = K\frac{\partial^2 h}{\partial x^2} + \frac{\partial K}{\partial x}\frac{\partial h}{\partial x} \tag{7}$$

Applying central differences to all terms on the right side yields the following equation:

$$\Delta_t(h) = K\delta_x^2(h) + \delta_x(K)\delta_x(h) \tag{8}$$

Subtracting each side from the other should result in zero when the equation is solved, and any remaining error or residual describes how far from a solution our terms are. This residual equation is shown in Equation (9):

$$R_1 = K\delta_x^2(h) + \delta_x(K)\delta_x(h) - \Delta_t(h) \tag{9}$$

To improve stability, the model is solved implicitly using the Crank-Nicolson scheme, which averages current and future model states. This approach yields second-order accuracy in both time and space.

2.2.2. Treatment of the tracer advection equation

The discretization of Equation (2) follows the same finite difference approach as Equation (1). Expanding the temporal and spatial derivatives via the product rule, we obtain the following equation:

$$h\frac{\partial w}{\partial t} + w\frac{\partial h}{\partial t} = Kw\frac{\partial^2 h}{\partial x^2} + K\frac{\partial w}{\partial x}\frac{\partial h}{\partial x} + \frac{\partial K}{\partial x}w\frac{\partial h}{\partial x} \tag{10}$$

Similar to previous approaches, an active layer with constant thickness A is introduced (e.g., Rivenæs, 1992; Wei et al., 2013). This layer represents the vertical thickness at each location x where w is mobile within the sediments. Substituting the mixed layer depth A for h on the left side, applying forward differences for the temporal derivatives as in Equation (1), and central difference approximations to the $\partial^2 h/\partial x^2$ and $\partial K/\partial x$ terms, we are left with the fully expanded form as shown in Equation (11).

$$A\Delta_t(w) + w\Delta_t(h) = Kw\delta_x^2(h) + K\frac{\partial w}{\partial x}\delta_x(h) + \delta_x(K)w\delta_x(h) \tag{11}$$

For numerical stability, in the discretization of the $\partial w/\partial x$ term, we adopt a one-sided upwind approach (U, Eqn. (12); Wei et al., 2013). The direction of flow is determined by the sign of $-\partial h/\partial x$, ensuring that the tracer moves downslope, consistent with physical intuition. When the topography to the left of the current grid point (h_{i-1}^n) is greater than that to the right (h_{i+1}^n), the system is solved using a backward difference approximation (downslope upwind). In all other cases, where the slope increases to the right, a forward difference (upslope upwind) is used (see Equation (12)).

$$U_x(w) = \begin{cases} \nabla_x(w), & h_{i-1}^n > h_{i+1}^n \quad \text{(downslope)} \\ \Delta_x(w), & h_{i-1}^n \le h_{i+1}^n \quad \text{(upslope)} \end{cases} \simeq \frac{\partial w}{\partial x} \tag{12}$$

Equation (11) is in the form of a one-dimensional advection equation. Numerical stability improves when the discretized domain of dependence aligns with the true advective domain (e.g., Wei et al., 2013). In other words, advection should be solved using a finite-difference approach that incorporates information exclusively from the upwind direction of the advecting signal.

A residual is defined as in Equation (1), where any remaining error quantifies the deviation from a solution (Eqn. (13)):

$$R_2 = Kw\delta_x^2(h) + KU_x(w)\delta_x(h) + \delta_x(K)w\delta_x(h) - A\Delta_t(w) - w\Delta_t(h) \tag{13}$$

2.3. Solving the approximated system for a single timestep

An iterative, Newton-Raphson approach is used to find a stable solution to our system of equations:

$$J(c^n)\,\Delta c = -R(c^n) \tag{14}$$

Here, c^{n+1} represents the h and w values at all grid points for the future time step of the model, c^n represents the h and w values at all grid points for the current model time step, and Δc represents the change in our guess ($\Delta c = c^{n+1} - c^n$). J is a matrix containing the first order partial derivatives of the residual equations with respect to both h and w guesses (a Jacobian matrix), and $R(c^n)$ represents the residual of the system of equations. For each iteration, a new Δc is computed and applied to update both h and w simultaneously. The process repeats, recalculating the total residual magnitude after each update, until it falls below a defined threshold. This tolerance is applied to the full residual vector, which includes both h and w components.

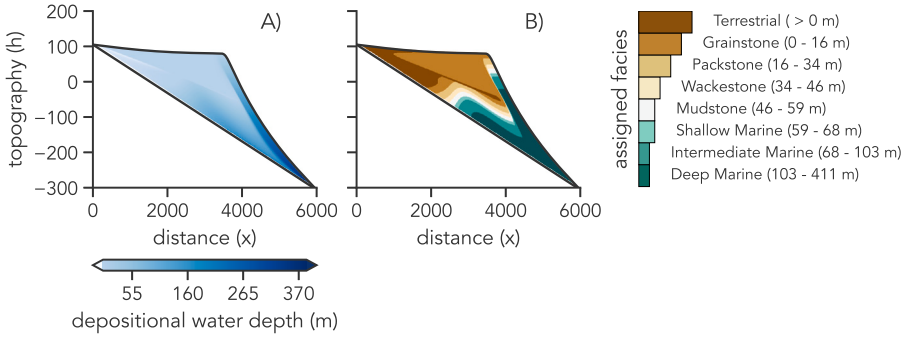

Fig. 2. Demonstration of facies binning method. Gridded water-depths are shown within the simulated basin in (A), and predicted facies based on the depth ranges relative to maximum simulated water depth are shown in (B). Vertical stratigraphic sections for all simulations in this study are generated using these predicted facies. Note that y-axis topographic units are relative to the initial sea-level prescribed, whereby the initial sea-level elevation is 0 m.

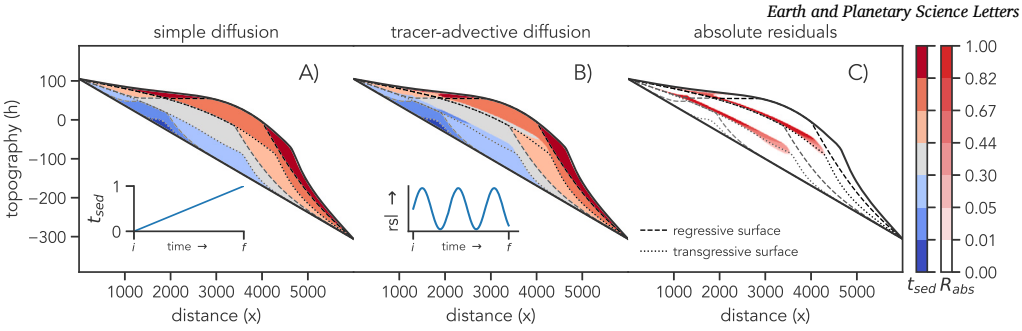

Fig. 3. Results from a model run with a simple sinusoidal sea-level forcing. Basins are colored by normalized particle age (the time the sediment was created) between 0 and 1. Transgressive and regressive surfaces are shown in dotted and dashed lines respectively. A model run with only the traditional diffusion equation (Eqn. (1)) is shown in (A), and a model run with coupled equations (Eqn. (1) and (2)) is shown in (B). Absolute values of residuals R between these simulations are shown with red in (C). A non-linear color bar scale is used for all panels. Note that y-axis topographic units are relative to the initial sea-level prescribed, whereby the initial sea-level elevation is 0 m.

2.4. Model components and parameters

2.4.1. Sediment production

To simulate the growth of carbonate sediments, we represent photosynthetic calcifiers using light-limited production curves modified and scaled from Bosscher and Schlager (1992) (Fig. 1). Using this method, multiple carbonate production curves can be combined to simulate carbonate growth within the model. When the conservative tracer w is considered to be the δ^{13}C value of carbonate, each type of produced carbonate is assigned a fractionation value (ϵ) that offsets its δ^{13}C value from the local "seawater DIC" value (e.g., the δ^{13}C value assigned to the grid point in which the carbonate grew).

2.4.2. Relative sea-level change and variable diffusivity

User-defined sea-level curves (e.g., Fig. 3B inset) provide the difference between sea-level and topography used to calculate water depth (z) and corresponding depth-dependent sediment diffusivity (Eqn. (15)). Diffusivity varies hyperbolically between two end-member values (subaerial diffusivity, K_a and subaqueous diffusivity, K_b) using topography h, sea-level S, and a smoothing factor γ (Fig. S1).

$$K = \frac{1}{2}\left[(K_a + K_b) - \tanh\left(\frac{h-S}{\gamma}\right)(K_b - K_a)\right] \tag{15}$$

2.4.3. Extracting predicted stratigraphy

To visualize modeled stratigraphy, an x-y grid is defined where x represents horizontal position and y represents depth. The final stratigraphic expression reflects net accumulation at each grid point, accounting for time steps when topography decreased and earlier sediments were removed. Depositional water depth (Fig. 2) is mapped at each timestep to idealized facies bins (e.g., 0.5-2.5 m for wackestone; Fig. 2B), producing facies-colored stratigraphic sections. Tracer values (e.g., δ^{13}C) are similarly recorded for each preserved layer.

2.5. Simulations

This model allows for the tracking of conservative tracers through deposition, subsequent erosion, and redeposition. With simple hillslope diffusion (Fig. 3A), a "proxy" value is assigned to each layer in the basin (here, colored by particle age t_{sed}, the time the sediment was created) at the time of deposition, based on its horizontal position in the model. If that layer is later eroded, the model loses any memory of its assigned proxy value. Importantly, the introduction of Equation (2) allows for the spatial advection of this proxy signal throughout the basin (Fig. 3B), better representing the behavior of conservative tracers in sediments that are created, eroded and re-deposited elsewhere in the basin. Without this additional proxy advection, critical nuances in the chemostratigraphic record are lost, and the model fails to reproduce the geochemical patterns expected under varying depositional conditions. Differences between the coupled equation approach (Eqn. (1) and (2)) introduced here, and simulations using only Equation (1) are clear and predictable (Fig. 3C). These differences reflect the difference in t_{sed} between panels A and B. Basin locations with higher residuals (R) are associated with transgressive surfaces, underscoring the limitations of using a single diffusion equation for sediment transport.

Table 1
List of simulated basin scenarios. Simulations are performed using either gradients in $\delta^{13}C_{DIC}$ with water depth (gradient driven scenarios) or with secular changes (excursions) in $\delta^{13}C_{DIC}$. In the case of secular excursions, the presented value represents the magnitude difference from expected deep-marine DIC values.

Model	Description	$\delta^{13}C_{DIC}$ (‰)		
		Shallow Water	Deep Water	Secular Excursion
1	Particle age	-	-	-
2	Gradient driven	6	1	-
3	Secular excursion	1	1	5
4	HICE simulation 1	4	0.5	-
5	HICE simulation 2	-	-	4
6	HICE simulation 3	3.5	0.5	2.5

To demonstrate the effects of sequence-stratigraphic architecture and different modes of isotopic variability (spatial gradients and temporal change), we explore several model scenarios summarized in Table 1. These include (1) an exploratory run using *Particle age* as a tracer (Fig. 3), (2) a *Gradient-driven* scenario with onshore-offshore $\delta^{13}C_{DIC}$ gradients (shallow > deep) and no secular change, and (3) a *Secular excursion* with a transient DIC shift but no spatial gradient. Scenarios (4)-(6) simulate basin conditions capable of generating the HICE.

3. Results

3.1. Redeposition of sediments: the distortion of time in sedimentary successions

Simulations show that sediment redistribution can deposit older material atop younger strata, creating age inversions in the stratigraphic record. Here, age refers to the original time of carbonate formation, which may preserve distinct geochemistry. When reworked sediments differ isotopically from newly formed carbonates, their emplacement produces a short-lived isotopic excursion, indistinguishable from one driven by secular DIC change. To examine this process, we track carbonate precipitation age (particle age) and compare it to depositional age.

As shown in Fig. 4A and C, under sea-level favoring progradation and retrogradation, particle age increases monotonically with vertical stratigraphic height. In other words, the final depositional age of the preserved sediment matches the precipitation age of the carbonate sediment. Conditions favoring sedimentary aggradation, through the stacking of multiple regressive sequences (Fig. 4B), are similarly found to

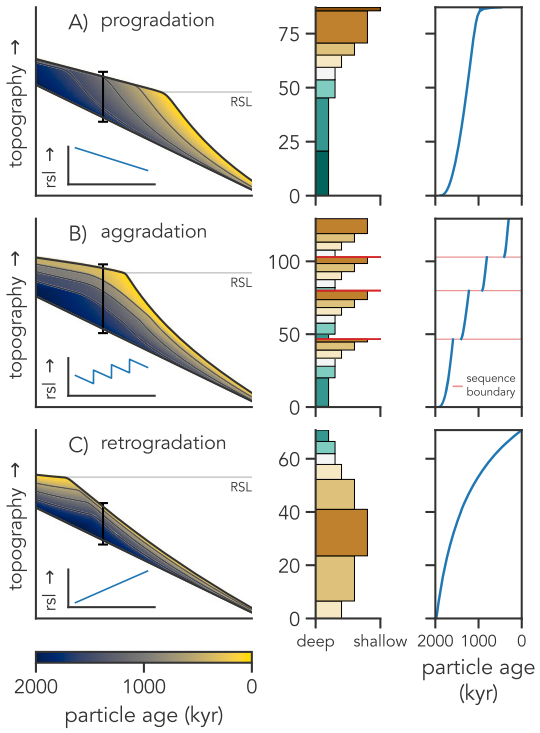

Fig. 4. Preserved stratigraphic records from three depositional systems highlighting the preservation of particle age. A basin scenario during progradation associated with gradual sea-level fall is shown in (A), a scenario undergoing net aggradation (through stacked regressive cycles) is shown in (B), and a sediment-starved retrogradational scenario associated with gradual sea-level rise is shown in (C). Each basin cross section is color-coded by particle age. Further, each model is paired with a representative stratigraphic column, derived from depositional water depths (binned to facies; see Fig. 7), taken from the marked location in each basin, along with the corresponding record of particle age. Sequence boundaries associated with aggrading cycles are shown in (B). Note that in all scenarios, particle age increases monotonically with stratigraphic height.

maintain monotonic vertical changes in particle age. However, under these conditions, the generation of hiatuses at sequence boundaries creates a fragmented record of particle age with step-wise jumps occurring across these surfaces as transgressive sequences are lost to erosion.

A change from a steady or seaward-moving shoreline, to one migrating landward (shoreline transgression) leads to conditions causing inversions between particle age and depositional age. Simulations predict that these inversions in sediment age are stratigraphically preceded by a sequence boundary generated through erosion during shoreline transgression (Fig. 5D). During erosion and subsequent redeposition, older sediments are eroded and redeposited atop younger sediments as a wedge of reworked material concentrated along and largely above the erosional surface (see Fig. 5A-C). The sediments immediately above the transgressive surface are likely deposited in a high-energy, shore-proximal setting during landward shoreline migration; they are typically coarse-grained and span the transition from late regression into early transgression, though the preserved stratigraphy is dominated by transgressive deposits. Thus, transgressive sequences most likely preserve the effects of redeposited beds and their geochemistry. Unconformities and erosive reworking are concentrated in shallow, shore-proximal settings and strongly affect preservation (e.g., fossil removal and stratigraphic redistribution; Holland, 2020). Similarly, reworking effects on geochemical records are most likely preserved in shallow deposits.

3.2. The lateral expression of gradient-generated carbon isotope excursions

Our model demonstrates that transport and redeposition can violate Steno's Law of superposition, motivating consideration of their broader chemostratigraphic implications. Because sediment geochemistry varies across time and space, transport transforms lateral gradients or temporal shifts in $\delta^{13}C_{DIC}$ into vertical isotopic trends. To explore this, we model stratigraphy along a shelf-to-slope transect reflecting the discrete stratigraphic sections available to stratigraphers. It is well established that $\delta^{13}C_{DIC}$ varies spatially throughout the ocean (e.g., Kroopnick, 1985), and particularly in nearshore settings (Weber and Woodhead, 1971; Patterson and Walter, 1994; Swart et al., 2009; Carvalho et al., 2015; Richardson et al., 2017) leading to variability in $\delta^{13}C_{carb}$. On the Great Bahama Bank, for instance, carbonates precipitate up to ~5‰ heavier than open-marine, pelagic slope sediments (Geyman and Maloof, 2019). Similarly, we simulate shallow carbonates precipitating at +6‰ and offshore carbonates at +1‰, matching this observed onshore-offshore offset (simulation 2; Table 1, Fig. 6, 7).

Results for the gradient scenario demonstrate that an isotopic excursion in $\delta^{13}C_{carb}$ is generated through the migration of facies belts, which carry distinct values of $\delta^{13}C$. As shown in Figs. 6C-D and 7B, an isotope excursion is created, with a magnitude matching that of the difference in isotopic composition between the shallow and deep carbonate end-members (here 5‰). Further, predictable patterns in the magnitude of the observed excursion are clear when examining a shore-proximal to shore-distal transect. Excursion magnitude is largest in intermediate depth settings (Fig. 7B), with magnitude decreasing away from shoreline. Such excursions can arise from basin-scale variations in local sea-level, meaning that those recorded in different basins may be asynchronous. Conversely, truly coincident excursions could reflect synchronous sea-level changes across multiple basins, potentially driven by a global sea-level signal.

Further discussion of the expression of gradient-driven excursions will be described in the context of vertical stratigraphy. In the most shore-proximal environments (Fig. 7A), vertical changes in $\delta^{13}C_{carb}$ are initially dominated by the $\delta^{13}C_{carb}$ values of deep-water carbonate end-member sediments likely to be fine-grained. Values within the regressive sequence increase throughout a shallowing upwards sequence, reflecting a transition towards the shallow carbonate end-member with elevated $\delta^{13}C_{carb}$ values, up to the transgressive surface marking the sequence boundary. Above the sequence boundary, coarse-grained, transgressive carbonates have elevated $\delta^{13}C$ values reflecting shallow-water deposition. Thus in the most shore-proximal settings, there is no expression of an isotope excursion, but rather a step-wise transition from deep to shallow geochemical end-members. In more intermediate settings (Fig. 7B), similar processes lead to the transition from shallow to deep end-members at a sequence boundary. However the occurrence of a second regressive sequence on top of the transgressive sequence yields a decrease in $\delta^{13}C_{carb}$ back from the maximum excursion magnitude ($\delta^{13}C_{carb}$ end-member difference) towards lighter values of the deep water end-member.

In distal settings (Fig. 7C), transgressive deposits bounded by regressive stratigraphy are still indicative of a shift from basinward to landward isotopic end-member values. However, the magnitude of the expressed excursion is dampened relative to the intermediate to proximal sections, indicating attenuation with increased distance from shore. Finally, the most basinward settings (Fig. 7D) are filled dominantly with deep-water carbonate sediments, with $\delta^{13}C_{carb}$ values largely ~1‰. Results here show increased vertical variability between adjacent samples, with the excursion magnitude much less than the maximum gradient, reflecting mixing with up-slope material.

Differences in $\delta^{13}C_{DIC}$ values between shallow and deep-water end-members provide sufficient vertical change to generate an isotope excursion with redeposited sediments. As shown in the region highlighted in grey in Fig. 7B, the coarsest-grained sediments are characterized by an abrupt drop in $\delta^{13}C_{carb}$ values away from the shallow end-member value, towards lower $\delta^{13}C_{carb}$ values, a phenomenon absent in more proximal or distal settings. This deviation appears stratigraphically above a sequence boundary (dotted red line in Fig. 7B) and represents the redistribution of older, previously deposited sediments with $\delta^{13}C_{carb}$

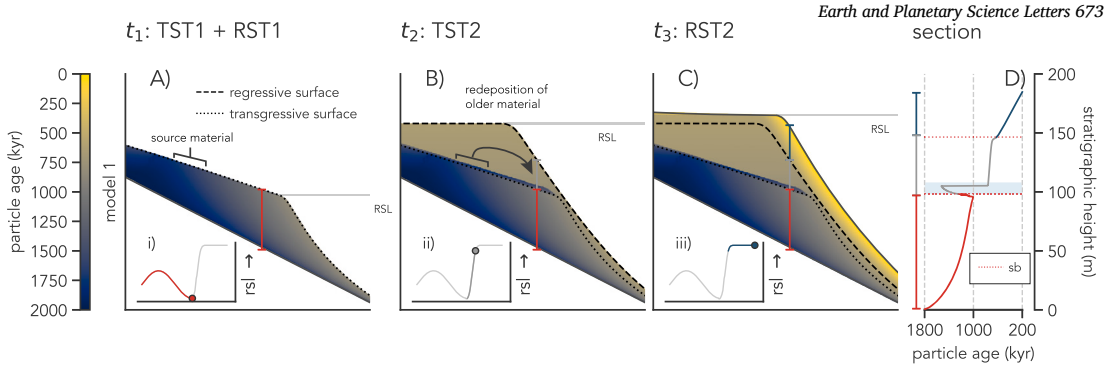

Fig. 5. Preservation of particle age (model 1, Table 1) shown as three basin snapshots, simulated under a sea-level forcing shown in the insets (i), (ii), and (iii) with colored segments indicating the time-span and system tracts preserved in the basin (RST = regressive system tract, TST = transgressive system tract). The sea-level for the basin snapshot shown in each panel is indicated by the colored circle along each curve in (i), (ii), and (iii). Surfaces marking the transgressive and regressive surfaces (sequence boundaries - SB) are shown with the dotted and dashed lines respectively in panels (A) through (C). These surfaces represent the topography present when the shoreline migration direction changed. Note that TST1 is of much smaller magnitude than TST2 and hence produces a negligible effect on the geochemical record.

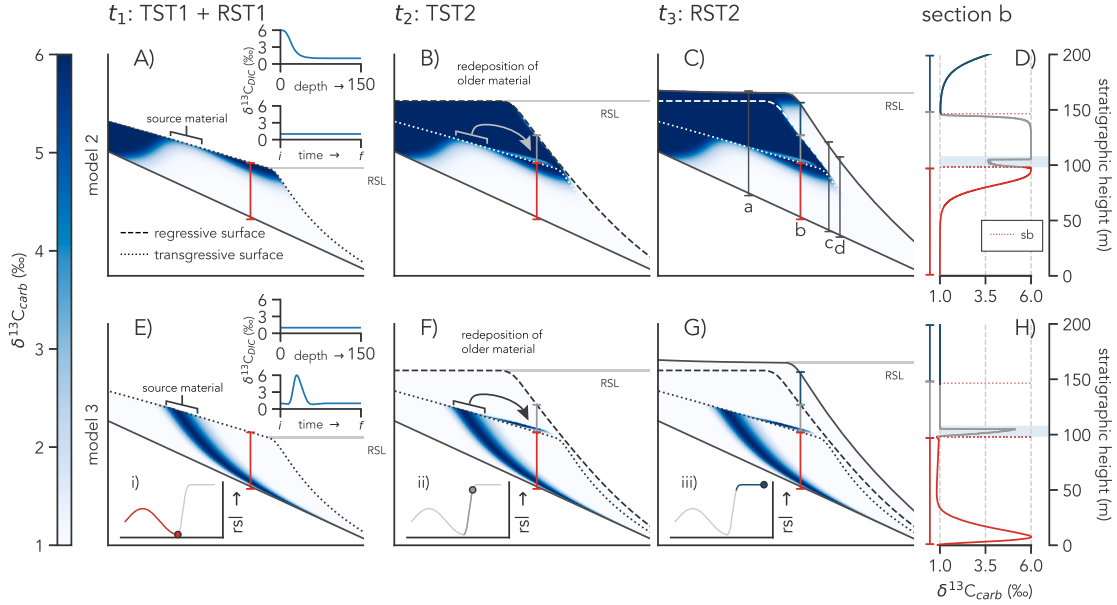

Fig. 6. Preserved $\delta^{13}C_{carb}$ composition of sediments in basins under two model scenarios (A)-(D) and (E)-(H). The depth gradients in $\delta^{13}C_{DIC}$ values and secular changes in $\delta^{13}C_{DIC}$ values imposed on each model scenario are shown as insets in panels (A, Model 2 from Table 1) and (E, Model 3 from Table 1). Panel (D) is an extracted chemostratigraphic profile from Model 2 (marked section *(b)* on panel C), and panel (H) is from Model 3 (marked on panel G). Modeled sea-level curves are shown in insets (i), (ii), and (iii) with colored segments indicating the timespan and system tracts preserved in each basin. The final timestep and sea-level for each panel is indicated by the colored circle along each curve. Isotopic excursions originating from the redistribution of previously deposited stratigraphy are highlighted in panels (D) and (H) in blue. Section lines *(a)* to *(d)* marked in grey in panel (C) refer to transect sections shown in Fig. 7. Note as in Fig. 5, that TST1 is of much smaller magnitude than TST2 and hence produces a negligible effect on the geochemical record.

values reflecting deeper water values (i.e., the mechanism described in Fig. 5). This "redepositional excursion" has an absolute magnitude in $\delta^{13}C_{carb}$ values generally less than the end-member difference, due to mixing with other sediments. Further, the direction of the excursion is opposite from the existing geochemical gradient within the basin. Namely, elevated $\delta^{13}C_{DIC}$ in shallow bank-top waters relative to deeper areas drives a basin-wide positive excursion, but the redepositional excursion, hosted in the shallowest facies, is a negative one.

From these model results, basin-scale stratigraphic trends in the magnitude of gradient-driven $\delta^{13}C_{carb}$ excursions show that excursions are obscured in proximal settings, dampened in distal settings, and maximized in intermediate settings. In the presence of only gradients and no secular variability in $\delta^{13}C_{DIC}$, an excursion in $\delta^{13}C_{carb}$ values can be generated through local sea-level driven transport of deep-water sediments with low $\delta^{13}C_{carb}$ values overtop of shallow-water sediments with higher $\delta^{13}C_{carb}$ values (Figs. 6A-D, 7B) up to the magnitude difference between the isotopic composition of shallow and deep-water end-members. Moreover, the most proximal and distal sections will reflect the geochemical end-member compositions for the shallow-water and deep-water end-members, respectively. Thus, the magnitude of gradient-driven isotope excursions scales with the range of depositional environments preserved in a stratigraphic sequence. In basin locations where all sediments are coastal (most landward) or all sediments are very deep (most distal), isotopes will be largely invariant (Fig. 7A and D). However, in the parts of basins where shallow-water sediments prograde over deeper-water sediments, the isotopic excursion will be maximized where the deepest and shallowest depositional environments are preserved in the same sequence, and the excursion should decrease in magnitude seaward of this region that marks the coastline's most seaward extent. Gradient-driven isotope excursions in intermediate settings are capped by marine flooding surfaces and, if erosion during the regression-transgression transition is sufficient, can be associated with

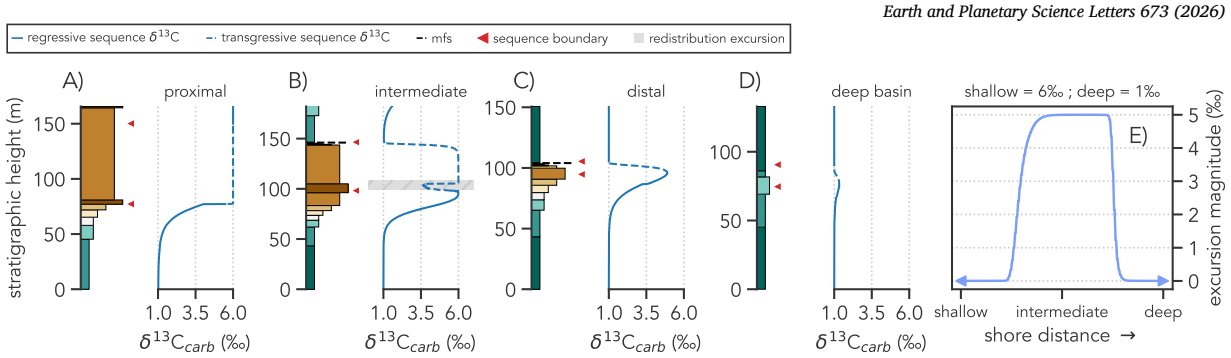

Fig. 7. Model scenario run with an isotopic depth gradient (most positive in shallow waters and decreasing isotopically with water depth) and no secular change to marine DIC. Panels, ordered by increasing distance from the coastline, show stratigraphic sections colored by depth-binned facies from proximal (A), intermediate (B), distal (C), to deep basin (D). Note the generation of a redepositional excursion highlighted in grey in panel (B, see also Fig. 6). The $\delta^{13}C_{carb}$ profile in each panel is further split into values sourced from both regressive sequences (solid lines) and transgressive sequences (dashed lines). Surfaces including sequence boundaries and maximum flooding surfaces (MFS) are highlighted. Water depths associated with each "facies" is shown in the stratigraphic legend in Fig. 2. Panel (E) shows a plot of excursion magnitude (the difference between baseline and maxima for areas that have a perceivable excursion - a rise, plateau, and a fall) and shoreline position. Data shown in sections is taken from the locations that mark a shift from shallow-water carbonate dominated sections, to deep-water carbonate dominated sections and occurs in-between intermediate and deep-basin environments. Note that in regions both shore-ward and basin-ward of intermediate settings, $\delta^{13}C_{carb}$ excursion magnitude approaches zero.

sequence boundaries (Fig. 7B and C). If erosion is limited, the transition from deep to shallow-water end-members is gradual, and no distinct excursion is preserved. Additionally, redepositional excursions related to the redistribution of older sediments are always found in association with sedimentation occurring in the latest stages of shoreline regression and through the initial stages of transgression along erosive surfaces and sequence boundaries.

Geochemical gradients that exist across the modern platform-top environment will exist in the rock record as stratigraphic excursions, reflecting spatial variability transformed into vertical trends. This concept parallels Walther's Law, where laterally adjacent environmental conditions are recorded vertically in the stratigraphy, a concept that could be thought of as "Walther's Law of Isotopes" (e.g., Geyman and Maloof, 2021). These types of excursions cannot have magnitudes that exceed the gradient observed in the modern environment, and excursion magnitudes will decrease basinward due to mixing with deeper-water sediments. Additionally, the excursion should covary with depositional environment (at least to the degree that identifiable facies correspond to distinct geochemical settings) and the maxima (or minima) of the excursion will display a predictable relationship to sequence boundaries. If $\delta^{13}C$ values within a basin are controlled by coastline proximity, then the top of each regressive sequence will be characterized by the maximum magnitude of the excursion. These predictions represent expectations for any sedimentary system, and isotopic changes over time are only necessary to account for observations deviating from these predictions.

3.3. The redistribution of past isotopes

Isotopic change over time can produce stratigraphic variations that deviate from the expectations outlined above. In the simplest case, an isotopic excursion with a magnitude larger than local gradients is best explained by secular changes to marine DIC. Similarly, secular changes best explain excursions that do not correlate with facies or proximity to sequence boundaries. In basins with local variations in sea-level, sediments containing temporal excursions are expected to decrease in thickness progressively with distance into the basin, and may truncate landward into a sequence boundary. Importantly, transgressive deposits can host redepositional isotope excursions that form due to the redeposition of older material that originally contained a secular excursion. These redepositional excursions can result in duplication of the original isotopic excursion, with the duplicate consistently positioned at the base of the transgressive deposit.

To explore these ideas in the absence of onshore-offshore gradients, we model a secular isotope excursion with a magnitude of 5‰ in a basin model (model 3 in Table 1, Fig. 6E-H). To enable meaningful comparisons with model 2 (Table 1, Fig. 6A-D), we invoke the same sea-level forcing (Fig. 6, insets *i* through *iii*) for both models. The secular excursion is preserved throughout the regressive sequence shown in Fig. 6E. This excursion does not correlate with facies changes across the full range of water depths and is most condensed (i.e. preserved within the thinnest stratigraphy) in the most basinward position. Moving forward in time, Fig. 6F illustrates that the preserved excursion occurs independently of sequence boundaries. However, shoreline movement during late-stage regression and onset of transgression creates an eroded wedge of sediments that is reworked downslope, moving material containing the +5‰ excursion overtop of sediments containing post-excursions $\delta^{13}C_{carb}$ values. This redepositional excursion is found to concentrate in sediments near the transgressive surface which, here, corresponds to a sequence boundary. Notably, the redepositional excursion is a secondary duplication of the original, primary isotope excursion. Additionally, the magnitude of the duplicate excursion is dampened relative to the original. As the remaining sediments in the preserved chemostratigraphic section are stacked, a pattern emerges whereby the primary excursion, matching the $\delta^{13}C_{DIC}$ shift in magnitude, occurs within the regressive sequence and is overlain by a transgressive sequence containing a lower-magnitude redepositional duplicate (Fig. 6H). Key findings from this result are threefold: *1)* as with the gradient-driven simulations (model 2, Table 1), redepositional excursions unrelated to changes in local basin processes or open marine DIC are preserved predominantly in transgressive deposits, *2)* when occurring at any point during shoreline regression, secular excursions in marine DIC can become duplicated, presenting as *double-pulsed* excursions within stratigraphically younger material, and *3)* the second isotopic excursion is asynchronous with the original excursion, appearing in different stratigraphic sequences through reworking of sediments containing the "true" excursion and concentrating above the erosive surface or within the basal deposits of the overlying transgressive sequence. In summary, the magnitude and preservational environment of the duplicated redepositional excursion follow predictable patterns, and these can be used to aid in distinguishing a primary vs duplicated excursion in the geologic record.

4. Discussion

Our model results show that the isotopic composition of sediments is tightly linked to their stratigraphic architecture. Thus, sediment source and transport must be considered when explaining isotopic variabil-

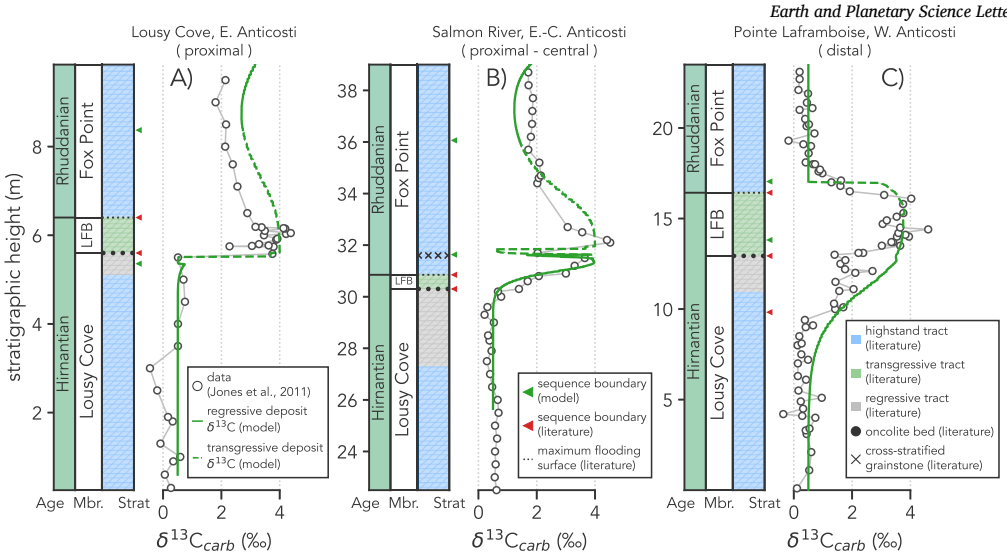

Fig. 8. Results of a model scenario run with a gradient-driven scenario whereby shallow carbonate sediments are 4‰ heavier than deep-water sediments. A sea-level curve is applied whereby an ~150 m drop in sea-level occurs (Finnegan et al., 2011; Creveling et al., 2018), followed by a rise back to baseline values to simulate the approximate conditions during the Hirnantian glaciation (Kump et al., 1999). Data is plotted along a simulated shore to basin transect where the most shore-proximal data is plotted in (A) and the most shore-distal data is shown in (C). Coupled with the model data, three sections from Anticosti Island (Jones et al., 2011) are plotted (white scatter points) at their respective approximate paleo-basin locations along the transect from proximal (Lousy Cove) to Distal (Pointe Laframboise). Approximate sequence stratigraphy for each of the Anticosti sections is shown alongside each dataset, with significant unconformable sequences and depositional environment noted (Jones et al., 2011; Zimmt et al., 2024). Each section is plotted relative to the member of the Ellis Bay Formation (Hirnantian, comprised of Lousy Cove Member and Laframboise Member - LFB), and the lowermost Becscie Formation (Silurian, Fox Point Member).

ity. Migration of lateral $\delta^{13}C_{DIC}$ gradients can produce isotope excursions whose magnitude and form vary spatially. These excursions are strongest in intermediate settings, where transgressive and regressive sequences are both preserved, and dampened or absent in proximal and distal settings. Redepositional excursions arise during late regression and early transgression along erosional surfaces and sequence boundaries. We show that secular marine DIC excursions can be duplicated near sequence boundaries through reworking of older sediments, producing double-peaked signals. Together, these results highlight the importance of stratigraphic context in interpreting marine carbonate $\delta^{13}C$ records and provide insight into the processes that generate isotopic excursions.

4.1. Case study: variability of the HICE on a shelf to slope transect in eastern Canada

To demonstrate this framework's relevance to $\delta^{13}C$ excursions, we apply it to the HICE in Laurentia: a positive $\delta^{13}C_{carb}$ excursion with magnitudes up to 7‰ (Melchin et al., 2013), coinciding with the onset of Hirnantian glaciation and sea-level fall (Melchin and Holmden, 2006). Proposed mechanisms include increased organic carbon burial (Brenchley et al., 1994), isotopically distinct riverine input from enhanced carbonate weathering (Kump et al., 1999), and spatial variability in DIC and mineralogy coupled with early marine diagenesis (Jones et al., 2020).

Variations in the magnitude and timing of the HICE are observed across different basins (Melchin et al., 2013; Jones et al., 2015, 2016). Additionally, evidence suggests the presence of gradients exceeding 4‰ in marine $\delta^{13}C_{DIC}$ between shallow and deep environments (Melchin and Holmden, 2006; LaPorte et al., 2009; Yang et al., 2024), and reflected in the variability of excursion magnitudes within studied basins (LaPorte et al., 2009). To investigate the expression of the HICE, we focus on Anticosti Island in Quebec, Canada, which is uniquely situated to explore the spatial variability of the HICE. Outcrops across Anticosti in a west to east direction constitute a shelf-to-slope transect, from shallow eastern settings to deeper, distal environments in the west (Jones et al., 2011). This geometry makes Anticosti Island ideal for exploring how local transport affects HICE expression. We impose a depth-gradient in $\delta^{13}C_{DIC}$ of 4‰ (simulation 4, Table 1) on a basin with a simplified sea-level curve that will replicate the observed sequence stratigraphy of the Hirnantian (Kump et al., 1999).

4.2. The migration of gradients and HICE generation

We hypothesize that the migration of spatial gradients in marine $\delta^{13}C_{DIC}$ can produce vertical trends in $\delta^{13}C_{carb}$ similar to those associated with the HICE (Fig. 8). The presence of basin-scale gradients have been previously suggested to explain at least a component of the total magnitude of the HICE (Jones et al., 2020; Yang et al., 2024), though these studies also invoke other, non-primary processes (such as diagenesis) simultaneously. We selected three stratigraphic sections along a proximal-to-distal transect on Anticosti Island (Fig. 8; Jones et al., 2011) to assess how depositional environment influences the expression of the HICE. Across all sections, the HICE begins during regression and peaks during transgression, though its structure and magnitude vary spatially. The excursion is stratigraphically confined between two erosive surfaces, with the lower surface marking a major sequence boundary; the HICE maximum is consistently preserved within the intervening transgressive deposits. In the proximal section (Fig. 8A), $\delta^{13}C_{carb}$ values rise sharply from a 0.5‰ baseline to a 4‰ maximum found in an oncolite bed, a stratigraphic horizon that is traceable across the island (Jones et al., 2011), while in central (Fig. 8B) and distal (Fig. 8C) sections, the transition is more gradual, and the distal section lacks a step-wise jump. The oncolite bed, interpreted as a transgressive lag (Jones et al., 2011), varies in thickness along the transect but consistently hosts the HICE maximum, linking a facies transition to the isotopic excursion. Following the peak, $\delta^{13}C_{carb}$ values fall to a post-HICE baseline of ~2‰ in proximal and central sections, while the distal section returns to a lower baseline of ~0.5‰. These patterns suggest a facies-dependent signal, with platform-proximal settings preserving more amplified excursions and isotopically heavier post-HICE values, likely due to their proximity to the shoreline and variation in accommodation space.

Spatial patterns in the HICE on Anticosti Island are well explained by model simulations with no secular DIC shift and a depth-dependent $\delta^{13}C_{carb}$ gradient. An imposed 3.5‰ $\delta^{13}C_{DIC}$ gradient coupled with local sea-level fall reproduces the chemostratigraphic patterns observed

on Anticosti Island (LaPorte et al., 2009; Yang et al., 2024), as transgression deposits shallow-water carbonates (~4‰) over deeper sediments (0.5‰, reflecting open-marine DIC), with the resulting excursion enclosed by sequence boundaries in matching stratigraphic positions (Fig. 8). Additionally, our model predicts that proximal sections experience increased hiatuses and/or erosion, an observation consistent with data from proximal sections on Anticosti (Jones et al., 2011) where sections record significantly smaller magnitudes of $\delta^{13}C$ change and stepwise shifts across sequence boundaries (Fig. 8A). In these settings, post-excursion values in upper transgressive deposits are expected to have isotopic values heavier than those of the lower regressional package, as these sediments generally form in closer proximity to the coastline, consistent with the pattern on Anticosti (Fig. 8).

In more intermediate settings, model results predict the retention of higher post-excursion $\delta^{13}C_{carb}$ values but with a gradual onset to an excursion maximum, which coincides with a sequence boundary. Sedimentary reworking along the lower sequence boundary, associated with sea-level fall, generates redepositional excursions superimposed on the larger-scale excursion (Fig. 7). Such an excursion may explain the observed ~2‰ drop in $\delta^{13}C_{carb}$ observed over short vertical ranges in the cross-stratified grainstones (~32 m up-section, Fig. 8B, Jones et al., 2011).

We find that in distal settings (Fig. 8C), a gradual rise to peak excursion values is expected before returning to baseline values characteristic of deep-water sedimentation (~0.5‰, Fig. 7C-D). These patterns, both in excursion magnitude and proximity to transgressive deposits bounded by sequence boundaries, are consistent with observations from Anticosti Island. Moreover, a gradient-driven excursion such as this should exhibit facies-dependent variations in $\delta^{13}C_{carb}$, as evidenced by the association of HICE maxima with shallow-water deposition and transgressive deposits. This suggests that the migration of isotopically distinct local gradients alone could generate an excursion remarkably similar to the HICE, even in the absence of a secular shift in marine DIC.

We have shown with our model that the maximum magnitude of such excursions cannot exceed the magnitude of the existing $\delta^{13}C_{DIC}$ gradient (Fig. 7), and may match it fully if the stratigraphic section samples the complete range of depositional facies within the basin. Thus, if the HICE were generated in part by transport and redistribution of isotopically distinct sediments, its magnitude could reflect the spatial structure of $\delta^{13}C_{DIC}$ across the basin, rather than a global change in the $\delta^{13}C$ value of DIC. Workers often argue that consistent HICE maxima within sampled basins imply the absence of spatial gradients in $\delta^{13}C_{carb}$. However, if measured sections are from a limited set of depositional settings (i.e., just intermediate depths), maximum excursion magnitude may appear invariant even in the presence of a spatial $\delta^{13}C_{DIC}$ gradient. While this model likely does not offer an explanation for all observations of the HICE, we use this as an illustrative example of how physical transport and redistribution can be related to excursions in $\delta^{13}C_{carb}$. Variability unexplained by gradients alone can be explained through secular changes in marine DIC or diagenetic reactions. Further, these findings highlight how transport may play an underappreciated role more broadly in the expression of $\delta^{13}C_{carb}$ records throughout geologic time.

4.3. A secular origin for the HICE

The idea that local transport contributes to the HICE is not incompatible with the possibility of global processes also contributing to the excursion. Several features of the excursion cannot be explained with local processes alone. For example, the HICE is observed globally, including eastern and arctic Canada (Jones et al., 2011; Melchin and Holmden, 2006), Europe (Kaljo et al., 2004; Ebbestad et al., 2015), the Great Basin, USA (Jones et al., 2016), South China (Yan et al., 2009), and Russia (Kaljo et al., 2012). Global eustasy, linked to glaciation, could drive similar and coincident migration of facies/isotopic belts across these regions. Additionally, such a climatic shift could coincide with

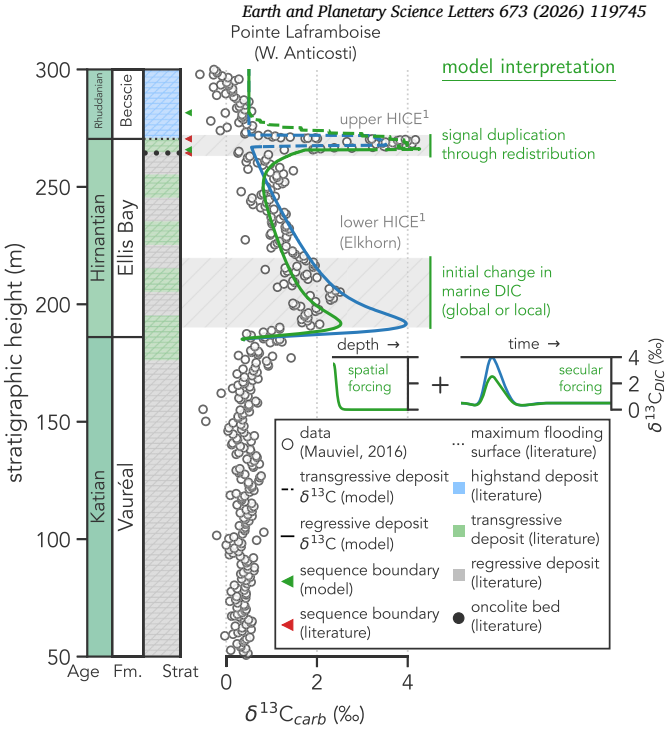

Fig. 9. Data from a stratigraphic section near Pointe Laframboise (western Anticosti Island) spanning Katian through Rhuddanian sediments, including both the lower HICE (Elkhorn excursion) and the upper HICE (Mauviel and Desrochers, 2016). Representative sequence stratigraphy is shown, compiled from Jones et al. (2011); Desrochers et al. (2010); Zimmt et al. (2024) for the Ellis Bay and Becscie formations, and from McLaughlin et al. (2016) for the Vauréal Formation. To replicate a double-pulsed HICE, we run two model simulations. The first (blue curve; model 5 in Table 1) imposes a 4‰ secular shift in $\delta^{13}C_{DIC}$. The second (green curve; model 6 in Table 1) combines a 2.5‰ secular shift in open-marine DIC with a 3.5‰ gradient-driven shift in shallow DIC to account for the high magnitude of the upper HICE. Note the stratigraphic position of the oncolite bed (interpreted as a transgressive lag; Jones et al., 2011) relative to the upper HICE.

changes in the global carbon cycle. Building on this idea, we examine how global signals and local sediment transport may interact to generate key features of the HICE, such as its two-pulsed form (e.g., Mauviel and Desrochers, 2016; Jones et al., 2020).

As shown in Fig. 9, a section measured through sediments on western Anticosti demonstrates a consistent chemostratigraphic trend associated with the HICE (Mauviel and Desrochers, 2016). It is clear that baseline $\delta^{13}C_{carb}$ values of ~0.5‰ persist for much of the Katian, before rising in an excursion with a magnitude of ~2.5‰ (Mauviel and Desrochers, 2016). This excursion, referred to as the lower HICE (Melchin et al., 2013), persists over ~60 m of stratigraphy before returning to values of 0.5‰. Directly above oncolite deposits (as in Fig. 8), $\delta^{13}C_{carb}$ values rise over less than 20 m of stratigraphy to values exceeding 4‰. This second excursion (referred to as the upper HICE and corresponding to the excursion modeled previously) occurs within transgressive sediments (see Fig. 8) and is stratigraphically capped by a maximum flooding surface and highstand sediments with baseline $\delta^{13}C_{carb}$ values (0.5‰).

The stratigraphic position and thickness of both the upper and lower HICE match predictions from our model simulations (Fig. 9), but the magnitude of the excursions requires either a secular change in $\delta^{13}C_{DIC}$, amplified and duplicated by transport and the same type of spatial gradients described in the gradient-driven model previously, or that the lower HICE under-samples the true isotopic gradient during deposition. To simulate a double-pulsed $\delta^{13}C_{carb}$ excursion from a single perturbation, we invoke a 4‰ secular shift in DIC (model 5, Table 1, Fig. 9). This model demonstrates that an excursion derived from secular change in DIC can be eroded and redistributed provided a sufficiently large sea-

level fall is followed by a subsequent rise consistent with Hirnantian stratigraphic evidence. This mechanism could duplicate the excursion along a sequence boundary, where it is preserved in basal transgressive sediments such as the coarse-grained oncolite lag and overlying deposits. However, a shift in $\delta^{13}C_{DIC}$ matching the maximum HICE magnitude fails to match observations in two ways. First, the modeled 4‰ shift creates a lower HICE with a greater magnitude than that observed in the rock record (true magnitude of ~2.5‰, blue curve, Fig. 9). This discrepancy could reflect missing time in the record, but that seems unlikely given the absence of evidence for hiatuses (Mauviel and Desrochers, 2016; Jones et al., 2011). Second, the model predicts a larger initial pulse than the duplicate, a pattern not observed in either the sediment record or models with only a secular DIC shift. Instead, we observe facies-dependent variations in $\delta^{13}C_{DIC}$ during the upper HICE, consistent with an onshore-offshore gradient in shallow DIC.

Spatial variations in $\delta^{13}C_{DIC}$ can amplify or dampen secular changes in $\delta^{13}C_{DIC}$ in shallow settings. In this framework, deep-water sediments would retain open-marine DIC values and remain largely unaffected by shallow DIC changes induced by processes such as enhanced productivity. Thus, a 2.5‰ excursion in open-marine DIC would be preserved at the same magnitude in deep environments, while sediments deposited closer to the coastline would exhibit an additional offset driven by the spatial gradient. The larger upper HICE, interpreted as a redepositional duplicate, can be reproduced with a 2.5‰ open-marine shift and a 3.5‰ shallow gradient (green curve, Fig. 9). Under this interpretation, the upper HICE may be decoupled from contemporaneous shifts in open-marine DIC and may not directly reflect changes in global biogeochemical cycling. Additionally, the existing uncertainty in the relative timing of the upper and lower HICE may itself indicate that a simple, laterally continuous stratigraphy is not applicable. Age constraints derived from fossils or detrital minerals are subject to the same reworking processes that affect carbon isotopes, leading to stratigraphic averaging and possible age inversions. We note that a redepositional excursion would most likely be expressed in post-transgressive, coarse-grained deposits as described previously, although several Anticosti Island sections show HICE maxima preserved within strata containing bioherms, seemingly inconsistent with such an interpretation. However, the occurrence of bioherms within HICE-bearing strata is restricted to more distal settings (Jones et al., 2011), consistent with a scenario in which coarse, isotopically heavy material reworked upslope during transgression was transported into and stabilized within deeper, lower-energy settings where bioherms developed and incorporated or were cemented by this material.

Though our model captures broad sequence-stratigraphic trends, it omits several natural processes not captured by hillslope diffusion, including long-shore transport, storms, and channelized flow. The addition of such processes would likely increase shallow-water diffusivity and mixing, potentially homogenizing $\delta^{13}C_{carb}$ in the shallowest sediments. This would primarily alter local variance rather than geometry and is unlikely to affect the predicted spatial association between redepositional or gradient-driven excursions and sequence boundaries. Separately, the framework yields testable predictions for covariation between $\delta^{13}C_{carb}$ and $\delta^{13}C_{org}$ when both phases sample the same local DIC pool or are co-transported during reworking; excursions in $\delta^{13}C_{carb}$ driven by secular change are commonly paralleled by those in $\delta^{13}C_{org}$ (e.g., the upper HICE on Anticosti Island; Jones et al., 2011). Decoupling is expected when carbonate signals reflect mineralogical or diagenetic effects, or when erosion and redeposition remobilize carbonate after organic-matter loss.

5. Conclusions

Using a diffusive-advective model of sediment transport in shallow-basin settings, we explore the sequence stratigraphic preservation of $\delta^{13}C_{carb}$ signals in carbonate platform environments. In basins with strong spatial gradients in $\delta^{13}C_{DIC}$, isotopic excursions can be generated with magnitudes up to the difference between shallow and deep-water end-members. These excursions are facies-dependent and are likely to be enclosed by sequence boundaries. The direction of the excursion is controlled by the direction of the gradient (i.e., whether shallow DIC is heavier or lighter than open-marine DIC), while the magnitude of the excursion decreases basinward. In fully shallow water strata, no excursion is expressed, as the entire stratigraphy reflects the local shallow end member. Additionally, we show that the redistribution of underlying sediments with distinct $\delta^{13}C_{carb}$ compositions creates "redepositional excursions" found along major sequence boundaries, particularly within basal transgressive deposits that are likely to be coarse-grained.

The model further demonstrates that double-pulsed isotope excursions can arise from a single shift in marine DIC. If an initial excursion is preserved within deep-marine sediments, subsequent sea-level change can erode through these deposits and redeposit excursion-bearing sediments within transgressive deposits along a sequence boundary. This secondary excursion is expected to be asynchronous with the original excursion, and of a lower magnitude. We show that this mechanism can explain the double-pulsed HICE as recorded on Anticosti Island, Canada. Our results suggest that the most pristine records of global carbon cycle perturbations are most likely to be preserved in sections that lack sequence boundaries and erosive surfaces. In contrast, excursions found near sequence boundaries are more likely to contain artifacts from redeposition, and in some cases, the entire excursion signal could be redepositional in origin. Additionally, the relationships demonstrated here are scale-independent, with proportional changes in basin geometry or sea-level amplitude producing the same sequence-stratigraphic and isotopic patterns.

CRediT authorship contribution statement

Connor S. van Wieren: Writing – original draft, Visualization, Methodology, Investigation, Formal analysis, Conceptualization. **Blake Dyer:** Writing – review & editing, Supervision, Resources, Methodology, Conceptualization. **Jon M. Husson:** Writing – review & editing, Supervision, Resources, Conceptualization.

Declaration of competing interest

The authors declare that they have no known competing financial interests or personal relationships that could have appeared to influence the work reported in this paper.

Acknowledgements

The authors would like to acknowledge support from Natural Sciences and Engineering Research Council of Canada (NSERC) Discovery Grants to JMH (RGPIN-2022-03230), and BD (RGPIN-2021-04082).

Appendix A. Supplementary material

Supplementary material related to this article can be found online at https://doi.org/10.1016/j.epsl.2025.119745.

Code and data availability

All code and data required to reproduce the results of these analyses are accessible on Github (https://github.com/VanWieren/Paleozoic_CIEs).

References

Ahm, A.S.C., Bjerrum, C.J., Blättler, C.L., Swart, P.K., Higgins, J.A., 2018. Quantifying early marine diagenesis in shallow-water carbonate sediments. Geochim. Cosmochim. Acta 236, 140–159. https://doi.org/10.1016/j.gca.2018.02.042.

Algeo, T.J., 1996. Meteoric water/rock ratios and the significance of sequence and parasequence boundaries in the gobbler formation (middle Pennsylvanian) of south-central New Mexico. Geol. Soc. Am. https://doi.org/10.1130/0-8137-2306-X.359.

Allan, J., Matthews, R., 1982. Isotope signatures associated with early meteoric diagenesis. Sedimentology 29, 797–817. https://doi.org/10.1111/j.1365-3091.1982.tb00085.x.

Arthur, M.A., Schlanger, S.O., Jenkyns, H.C., 1987. The Cenomanian-Turonian Oceanic Anoxic Event, II. Palaeoceanographic Controls on Organic-Matter Production and Preservation. Special Publications, vol. 26. Geological Society, London, pp. 401–420.

Bosscher, H., Schlager, W., 1992. Computer simulation of reef growth. Sedimentology 39, 503–512. https://doi.org/10.1111/j.1365-3091.1992.tb02130.x.

Brenchley, P.J., Marshall, J.D., Carden, G.A.F., Robertson, D.B.R., 1994. Bathymetric and Isotopic Evidence for a Short-Lived Late Ordovician Glaciation in a Greenhouse Period.

Brown, C.N., Purkis, S.J., Gischler, E., Oehlert, A.M., 2025. Sedimentological Characterisation Is a Necessary Prerequisite for Interpretation of Stable Carbon Isotope Ratios of Bulk Sediment from Reefal Settings.

Caron, V., Nelson, C.S., Kamp, P.J., 2004. Transgressive surfaces of erosion as sequence boundary markers in cool-water shelf carbonates. Sediment. Geol. 164, 179–189. https://doi.org/10.1016/j.sedgeo.2003.10.001.

Carvalho, M.C., Santos, I.R., Maher, D.T., Cyronak, T., McMahon, A., Schulz, K.G., Eyre, B.D., 2015. Drivers of carbon isotopic fractionation in a coral reef lagoon: predominance of demand over supply. Geochim. Cosmochim. Acta 153, 105–115. https://doi.org/10.1016/j.gca.2015.01.012.

Creveling, J.R., Finnegan, S., Mitrovica, J.X., Bergmann, K.D., 2018. Spatial variation in Late Ordovician glacioeustatic sea-level change. Earth Planet. Sci. Lett. 496, 1–9. https://doi.org/10.1016/j.epsl.2018.05.008.

Curtis, A., Bloem, H., Wood, R., Bowyer, F., Shields, G.A., Zhou, Y., Yilales, M., Tetzlaff, D., 2025. Natural sampling and aliasing of marine geochemical signals. Sci. Rep. 15, 760. https://doi.org/10.1038/s41598-024-84871-6.

Desrochers, A., Farley, C., Achab, A., Asselin, E., Riva, J.F., 2010. A far-field record of the end Ordovician glaciation: the Ellis Bay Formation, Anticosti Island, Eastern Canada. Palaeogeogr. Palaeoclimatol. Palaeoecol. 296, 248–263. https://doi.org/10.1016/j.palaeo.2010.02.017.

Ebbestad, J.O.R., Anette, E.S.H., Åsa, M.F., Tõnu, M., Dimitri, K., Björn, K., Pärnaste, H., 2015. Terminal Ordovician stratigraphy of the Siljan district, Sweden. Gff 137, 36–56. https://doi.org/10.1080/11035897.2014.945620.

Finnegan, S., Bergmann, K., Eiler, J.M., Jones, D.S., Fike, D.A., Eisenman, I., Hughes, N.C., Tripati, A.K., Fischer, W.W., 2011. The magnitude and duration of late Ordovician–early Silurian glaciation. Science 331, 903–906. https://doi.org/10.1126/science.1200803.

Flessa, K.W., Jablonski, D., 1983. Extinction is here to stay. Paleobiology 9, 315–321. https://doi.org/10.1017/S0094837300007776.

Geyman, E.C., Maloof, A.C., 2019. A diurnal carbon engine explains ^{13} C-enriched carbonates without increasing the global production of oxygen. Proc. Natl. Acad. Sci. USA 116, 24433–24439. https://doi.org/10.1073/pnas.1908783116.

Geyman, E.C., Maloof, A.C., 2021. Facies control on carbonate δ13C on the Great Bahama Bank. Geology 49, 1049–1054. https://doi.org/10.1130/G48862.1.

Geyman, E.C., Wu, Z., Nadeau, M.D., Edmonsond, S., Turner, A., Purkis, S.J., Howes, B., Dyer, B., Ahm, A.S.C., Yao, N., Deutsch, C.A., Higgins, J.A., Stolper, D.A., Maloof, A.C., 2022. The origin of carbonate mud and implications for global climate. Proc. Natl. Acad. Sci. USA 119, e2210617119. https://doi.org/10.1073/pnas.2210617119.

Halverson, G.P., Hoffman, P.F., Schrag, D.P., Maloof, A.C., Rice, A.H.N., 2005. Toward a Neoproterozoic composite carbon-isotope record. Geol. Soc. Am. Bull. 117, 1181. https://doi.org/10.1130/B25630.1.

Henkes, G.A., Passey, B.H., Grossman, E.L., Shenton, B.J., Yancey, T.E., Pérez-Huerta, A., 2018. Temperature evolution and the oxygen isotope composition of Phanerozoic oceans from carbonate clumped isotope thermometry. Earth Planet. Sci. Lett. 490, 40–50. https://doi.org/10.1016/j.epsl.2018.02.001.

Higgins, J.A., Blättler, C.L., Lundstrom, E.A., Santiago-Ramos, D.P., Akhtar, A.A., Crüger Ahm, A.S., Bialik, O., Holmden, C., Bradbury, H., Murray, S.T., Swart, P.K., 2018. Mineralogy, early marine diagenesis, and the chemistry of shallow-water carbonate sediments. Geochim. Cosmochim. Acta 220, 512–534. https://doi.org/10.1016/j.gca.2017.09.046.

Holland, S.M., 2020. The stratigraphy of mass extinctions and recoveries. Annu. Rev. Earth Planet. Sci. 48, 75–97. https://doi.org/10.1146/annurev-earth-071719-054827.

Holmden, C., Kimmig, S.R., Nadeau, M.D., 2024. Ca isotopic gradients in epeiric marine carbonates: diagenetic origins of and significance for Ca cycle reconstructions. Geochim. Cosmochim. Acta 373, 151–168. https://doi.org/10.1016/j.gca.2024.03.017.

Jablonski, D., 1986. Evolutionary consequences of mass extinctions. In: Raup, D.M., Jablonski, D. (Eds.), Patterns and Processes in the History of Life. Springer Berlin Heidelberg, Berlin, Heidelberg, pp. 313–329.

Jones, D.S., Brothers, R.W., Crüger Ahm, A.S., Slater, N., Higgins, J.A., Fike, D.A., 2020. Sea level, carbonate mineralogy, and early diagenesis controlled δ13C records in Upper Ordovician carbonates. Geology 48, 194–199. https://doi.org/10.1130/G46861.1.

Jones, D.S., Creel, R.C., Rios, B., Santiago Ramos, D.P., 2015. Chemostratigraphy of an Ordovician–Silurian carbonate platform: δ13C records below glacioeustatic exposure surfaces. Geology 43, 59–62. https://doi.org/10.1130/G36236.1.

Jones, D.S., Creel, R.C., Rios, B.A., 2016. Carbon isotope stratigraphy and correlation of depositional sequences in the Upper Ordovician Ely Springs Dolostone, eastern Great Basin, USA. Palaeogeogr. Palaeoclimatol. Palaeoecol. 458, 85–101. https://doi.org/10.1016/j.palaeo.2016.01.036.

Jones, D.S., Fike, D.A., Finnegan, S., Fischer, W.W., Schrag, D.P., McCay, D., 2011. Terminal Ordovician carbon isotope stratigraphy and glacioeustatic sea-level change across, Anticosti Island (Quebec, Canada). Geol. Soc. Am. Bull. 123, 1645–1664. https://doi.org/10.1130/B30323.1.

Kaljo, D., Hints, L., Martma, T., Nõlvak, J., Oraspõld, A., 2004. Late Ordovician carbon isotope trend in Estonia, its significance in stratigraphy and environmental analysis. Palaeogeogr. Palaeoclimatol. Palaeoecol. 210, 165–185. https://doi.org/10.1016/j.palaeo.2004.02.044.

Kaljo, D., Männik, P., Martma, T., Nõlvak, J., 2012. More about the Ordovician–Silurian transition beds at Mirny Creek, Omulev Mountains, NE Russia: Carbon isotopes and conodonts. Est. J. Earth Sci. 61, 277. https://doi.org/10.3176/earth.2012.4.07.

Kaufman, P., Grotzinger, J.P., McCormick, D.S., 1991. Depth-dependent diffusion algorithm for simulation of sedimentation in shallow marine depositional systems. In: Bulletin (Kansas Geological Survey), pp. 489–508.

Kenyon, P.M., Turcotte, D.L., 1985. Morphology of a delta prograding by bulk sediment transport. Geol. Soc. Am. Bull. 96, 1457. https://doi.org/10.1130/0016-7606(1985)96<1457:MOADPB>2.0.CO;2.

Kroopnick, P.M., 1985. The distribution of 13C of ΣCO2 in the world oceans. Deep-Sea Res., A, Oceanogr. Res. Pap. 32, 57–84. https://doi.org/10.1016/0198-0149(85)90017-2.

Kump, L., Arthur, M., Patzkowsky, M., Gibbs, M., Pinkus, D., Sheehan, P., 1999. A weathering hypothesis for glaciation at high atmospheric pCO2 during the Late Ordovician. Palaeogeogr. Palaeoclimatol. Palaeoecol. 152, 173–187. https://doi.org/10.1016/S0031-0182(99)00046-2.

Kump, L.R., Arthur, M.A., 1999. Interpreting carbon-isotope excursions: carbonates and organic matter. Chem. Geol. 161, 181–198. https://doi.org/10.1016/S0009-2541(99)00086-8.

LaPorte, D., Holmden, C., Patterson, W., Loxton, J., Melchin, M., Mitchell, C., Finney, S., Sheets, H., 2009. Local and global perspectives on carbon and nitrogen cycling during the Hirnantian glaciation. Palaeogeogr. Palaeoclimatol. Palaeoecol. 276, 182–195. https://doi.org/10.1016/j.palaeo.2009.03.009.

Mauviel, A., Desrochers, A., 2016. A high-resolution, continuous δ13C record spanning the Ordovician–Silurian boundary on Anticosti Island, eastern Canada. Can. J. Earth Sci. 53, 795–801. https://doi.org/10.1139/cjes-2016-0003.

McLaughlin, P.I., Emsbo, P., Desrochers, A., Bancroft, A., Brett, C.E., Riva, J.F., Premo, W., Neymark, L., Achab, A., Asselin, E., Emmons, M.M., 2016. Refining 2 km of Ordovician chronostratigraphy beneath Anticosti Island utilizing integrated chemostratigraphy. Can. J. Earth Sci. 53, 865–874. https://doi.org/10.1139/cjes-2015-0242.

Melchin, M.J., Holmden, C., 2006. Carbon isotope chemostratigraphy in Arctic Canada: sea-level forcing of carbonate platform weathering and implications for Hirnantian global correlation. Palaeogeogr. Palaeoclimatol. Palaeoecol. 234, 186–200. https://doi.org/10.1016/j.palaeo.2005.10.009.

Melchin, M.J., Mitchell, C.E., Holmden, C., Storch, P., 2013. Environmental changes in the Late Ordovician-early Silurian: review and new insights from black shales and nitrogen isotopes. Geol. Soc. Am. Bull. 125, 1635–1670. https://doi.org/10.1130/B30812.1.

Muñoz-López, D., Koeshidayatullah, A., Bover-Arnal, T., Herlambang, A., Martín-Martín, J.D., Salas, R., Humphrey, J.D., Khalid, A.R., 2025. Isotopic record of Aptian third-order sea-level trends in platform margin carbonates: implications for sequence stratigraphic analysis. J. Sediment. Res. https://doi.org/10.2110/jsr.2024.124.

Patterson, W.P., Walter, L.M., 1994. Depletion of 13C in seawater ΣC02 on modern carbonate platforms: significance for the carbon isotopic record of carbonates. Geology 22, 885–888. https://doi.org/10.1130/0091-7613(1994)022<0885:DOCISC>2.3.CO;2.

Railsback, L.B., Holland, S.M., Hunter, D.M., Jordan, E.M., Diaz, J.R., Crowe, D.E., 2003. Controls on geochemical expression of subaerial exposure in Ordovician limestones from the Nashville Dome, Tennessee, U.S.A.. J. Sediment. Res. 73, 790–805. https://doi.org/10.1306/020503730790.

Richardson, C.M., Dulai, H., Popp, B.N., Ruttenberg, K., Fackrell, J.K., 2017. Submarine groundwater discharge drives biogeochemistry in two Hawaiian reefs. Limnol. Oceanogr. 62, S348–S363. https://doi.org/10.1002/lno.10654.

Rivenæs, J.C., 1992. Application of a dual-lithology, depth-dependent diffusion equation in stratigraphic simulation. Basin Res. 4, 133–146. https://doi.org/10.1111/j.1365-2117.1992.tb00136.x.

Sadler, P.M., 1981. Sediment accumulation rates and the completeness of stratigraphic sections. J. Geol. 89, 569–584. https://doi.org/10.1086/628623.

Salles, T., Duclaux, G., 2015. Combined hillslope diffusion and sediment transport simulation applied to landscape dynamics modelling. Earth Surf. Process. Landf. 40, 823–839. https://doi.org/10.1002/esp.3674.

Strasser, A., 2015. Hiatuses and condensation: an estimation of time lost on a shallow carbonate platform. Deposit. Record 1, 91–117. https://doi.org/10.1002/dep2.9.

Swart, P.K., 2008. Global synchronous changes in the carbon isotopic composition of carbonate sediments unrelated to changes in the global carbon cycle. Proc. Natl. Acad. Sci. USA 105, 13741–13745. https://doi.org/10.1073/pnas.0802841105.

Swart, P.K., Reijmer, J.J., Otto, R., 2009. A re-evaluation of facies on great Bahama bank II: variations in the Δ^{13} C, Δ^{18} O and mineralogy of surface sediments. In: Swart, P.K., Eberli, G.P., McKenzie, J.A., Jarvis, I., Stevens, T. (Eds.), Perspectives in Carbonate Geology, 1 ed. Wiley, pp. 47–59.

Tucker, G.E., Bras, R.L., 1998. Hillslope processes, drainage density, and landscape morphology. Water Resour. Res. 34, 2751–2764. https://doi.org/10.1029/98WR01474.

Uličný, D., Hladíková, J., Attrep Jr, M.J., Čech, S., Hradecká, L., Svobodová, M., 1997. Sea-level changes and geochemical anomalies across the Cenomanian–Turonian boundary: Pecínov quarry, Bohemia. Palaeogeogr. Palaeoclimatol. Palaeoecol. 132, 265–285. https://doi.org/10.1016/S0031-0182(97)00055-2.

van Wieren, C.S., Husson, J.M., Dyer, B., 2024. Chemostratigraphy of the Ediacaran Old Fort Point Formation in the southern Canadian Cordillera. Precambrian Res. 411, 107525. https://doi.org/10.1016/j.precamres.2024.107525.

Veizer, J., Ala, D., Azmy, K., Bruckschen, P., Buhl, D., Bruhn, F., Carden, G.A., Diener, A., Ebneth, S., Godderis, Y., Jasper, T., Korte, C., Pawellek, F., Podlaha, O.G., Strauss, H., 1999. $^{87}Sr/^{86}Sr$, $\delta^{13}C$ and $\delta^{18}O$ evolution of Phanerozoic seawater. Chem. Geol. 161, 59–88. https://doi.org/10.1016/S0009-2541(99)00081-9.

Weber, J.N., Woodhead, P.M.J., 1971. Diurnal variations in the isotopic composition of dissolved inorganic carbon in seawater from coral reef environments. Geochim. Cosmochim. Acta 35, 891–902. https://doi.org/10.1016/0016-7037(71)90003-2.

Wei, W., Clark, S.R., Su, H., Wen, M., Cai, X., 2013. Balancing efficiency and accuracy for sediment transport simulations. Comput. Sci. Discov. 6, 015011. https://doi.org/10.1088/1749-4699/6/1/015011.

Westerhold, T., Marwan, N., Drury, A.J., Liebrand, D., Agnini, C., Anagnostou, E., Barnet, J.S.K., Bohaty, S.M., De Vleeschouwer, D., Florindo, F., Frederichs, T., Hodell, D.A., Holbourn, A.E., Kroon, D., Lauretano, V., Littler, K., Lourens, L.J., Lyle, M., Pälike, H., Röhl, U., Tian, J., Wilkens, R.H., Wilson, P.A., Zachos, J.C., 2020. An astronomically dated record of Earth's climate and its predictability over the last 66 million years. Science 369, 1383–1387. https://doi.org/10.1126/science.aba6853.

Wignall, P.B., Benton, M.J., 1999. Lazarus taxa and fossil abundance at times of biotic crisis. J. Geol. Soc. 156, 453–456. https://doi.org/10.1144/gsjgs.156.3.0453.

Yan, D., Chen, D., Wang, Q., Wang, J., Wang, Z., 2009. Carbon and sulfur isotopic anomalies across the Ordovician–Silurian boundary on the Yangtze Platform, South China. Palaeogeogr. Palaeoclimatol. Palaeoecol. 274, 32–39. https://doi.org/10.1016/j.palaeo.2008.12.016.

Yang, S., Fan, J., Algeo, T.J., Shields, G.A., Zhou, Y., Li, C., Chen, J., Li, W., Li, N., Cao, J., Zhang, L., Sun, Z., Shen, S., 2024. Steep oceanic DIC δ13C depth gradient during the Hirnantian Glaciation. Earth-Sci. Rev. 255, 104840. https://doi.org/10.1016/j.earscirev.2024.104840.

Zachos, J., Pagani, M., Sloan, L., Thomas, E., Billups, K., 2001. Trends, rhythms, and aberrations in global climate 65 Ma to present. Science 292, 686–693. https://doi.org/10.1126/science.1059412.

Zachos, J.C., Röhl, U., Schellenberg, S.A., Sluijs, A., Hodell, D.A., Kelly, D.C., Thomas, E., Nicolo, M., Raffi, I., Lourens, L.J., McCarren, H., Kroon, D., 2005. Rapid acidification of the ocean during the Paleocene-Eocene thermal maximum. Science 308, 1611–1615. https://doi.org/10.1126/science.1109004.

Zimmt, J.B., Holland, S.M., Desrochers, A., Jones, D.S., Finnegan, S., 2024. A high-resolution sequence stratigraphic framework for the eastern Ellis Bay Formation, Canada: a record of Hirnantian sea-level change. Geol. Soc. Am. Bull. https://doi.org/10.1130/B37190.1.